

A Model-Based Trajectory Planning Method for Robotic Polishing of Complex Surfaces

Mubang Xiao, Ye Ding^{ID}, Member, IEEE, and Guilin Yang^{ID}, Member, IEEE

Abstract—Off-line programming of the polishing tool trajectory for complex workpieces is challenging due to the nontrivial material removal model and the polishing accuracy requirement. Current tool trajectory planning methods are mainly developed for some simple surfaces but cannot handle the increasingly complicated industrial parts, such as the wheel hubs. This article first develops a numerical contact mechanics model for the point-sampled complex workpieces. The contact pressure distribution and the material removal depths on the workpiece point cloud can be predicted efficiently. A novel high-priority subregion searching algorithm is developed to track the most-worth-polishing workpiece points. By selecting the path pattern as direction-parallel, the path direction, tool dwell times, and the path spacings inside each extracted subregion are optimized to minimize the deviation from the desired material removal depths. The effectiveness of the proposed method is verified by performing disk polishing simulations on workpieces with different shapes. A robotic polishing experiment is also conducted on a wheel hub. Both simulation and experimental results show that reasonable tool trajectories can be generated on the workpiece, and the desired material removal depths can be achieved.

Note to Practitioners—In robotic polishing industries, it is crucial to plan the tool trajectory (tool path and feed velocity) to achieve desired material removal depths on the workpiece surface, which means high surface quality. In this article, a model-based tool trajectory planning method for robotic polishing of complex surfaces that are represented by the point cloud form is presented. The advantage of using the point cloud is that workpiece surfaces with varying curvatures and complex features, e.g., grooves and holes, need not be expressed explicitly. The proposed method generates high-priority subregions according to the updated material removal distribution dynamically. In this work, the polishing path pattern is chosen as direction-parallel. Based on an efficient numerical contact mechanics and material removal model, the path locations and the tool dwell times inside each subregion are optimized to minimize the deviation between the

Manuscript received May 18, 2021; accepted June 28, 2021. This article was recommended for publication by Associate Editor B. Zhang and Editor K. Saitou upon evaluation of the reviewers' comments. This work was supported in part by the National Key Research and Development Program of China under Grant 2018YFB1308900 and in part by the National Natural Science Foundation of China under Grant 51822506 and Grant 91948301. (Corresponding author: Ye Ding.)

Mubang Xiao and Ye Ding are with the State Key Laboratory of Mechanical System and Vibration, School of Mechanical Engineering, Shanghai Jiao Tong University, Shanghai 200240, China (e-mail: xiaomb@sjtu.edu.cn; y.ding@sjtu.edu.cn).

Guilin Yang is with the Ningbo Institute of Materials Technology and Engineering, Chinese Academy of Sciences, Ningbo, Zhejiang 315201, China (e-mail: glyang@nimte.ac.cn).

Color versions of one or more figures in this article are available at <https://doi.org/10.1109/TASE.2021.3095061>.

Digital Object Identifier 10.1109/TASE.2021.3095061

actual and the desired material removal depths. When the desired material removal depths are attained in an extracted subregion, the algorithm finds the next high-priority subregion until the whole workpiece is well polished. The trajectory planning method can be integrated into an industrial robot with the force-control module. Future work is to integrate the roughness model into the tool trajectory planning method.

Index Terms—Complex surface, contact force modeling, path planning, robotic polishing.

I. INTRODUCTION

IN RECENT years, the robotic polishing systems with the force-control module have been widely applied to the surface finishing of freeform workpieces [1], [2], such as car bodies and wind turbine blades [3]. By maintaining the tool-workpiece contact force and programming the tool trajectories (i.e., the tool paths and tool feed velocities), overpolished or lack-polished phenomenons on the workpiece can be averted, which greatly improves the surface quality.

For the robotic polishing process focused on in our research, the goal is to achieve desired material removal depths on the workpiece. It shares some similarities with the robotic spray painting process [4], [5], where the spraying material should be uniformly deposited on the workpiece. The main characteristic of the material removal model is that the tool-workpiece contact force is positive and the contact pressure is nonzero within the tool-workpiece contact area. To predict the material removal depths on the workpiece surface, a specific contact mechanics model between the tool and workpiece should be developed. With the contact mechanics model, the material removal depths can be predicted by utilizing the classical Preston equation [6]. The Preston equation states that the longer time the polishing tool dwells at a workpiece point, the larger the material removal depth will have resulted.

When the material removal depths can be predicted, we can adjust the polishing tool trajectory (including tool feed velocity, path direction, and path location) and the polishing process parameters (including normal contact force and tool rotating speed) [29] to achieve desired material removal depths on the workpiece. As reported in the robotic polishing or spray painting studies [5], [7], there must be some simplifications of the planning procedure to reduce the number of variables that need to be optimized. Planning the tool trajectory is the most widely applied approach since it only needs to change the tool position. The tool trajectories are programmed offline and carried out by the industrial robot implementing the G-code.



Fig. 1. Wheel hub component and its point cloud.

The polishing process parameters are predetermined and set as constants during the polishing process. However, there are still a tremendous number of freedoms of the feed direction if it is allowed to vary along the polishing path all the time. To further simplify the tool trajectory planning problem, researchers have used fixed path patterns to cover the workpiece surface, and therefore, the path direction is restricted. The most popular path patterns are the direction-parallel path [8], [9] (or the so-called zig-zag path) and the spiral path [10], while the former pattern is most widely adopted in the robotic disk polishing industries.

For a workpiece with a large dimension and many complex features, e.g., the wheel hub in Fig. 1, it has multiple narrow spokes connecting its outer and inner rings. Besides, there are a large mounting hole and many small screw holes. It is not practical to generate direction-parallel paths in a single patch to cover the whole workpiece surface. Otherwise, the tool needs to frequently raise and drops to pass the grooves between spokes. Let us consider what will the human workers do to polish this complex workpiece. They may divide the wheel hub into multiple small patches, such as the spokes, the outer, and the inner rings, and then polish them sequentially. Of course, the surface division will change for different workpiece shapes. Determining the polishing sequence is also important. The human workers typically tend to polish workpiece points with a large reward, e.g., the redundant material depth defined in our polishing task later. Another important fact of human-like polishing is that human workers do not try to divide the workpiece surface into multiple patches with strict borders. Instead, they search the polishing regions iteratively. These characteristics are described in the high-priority subregion searching algorithm introduced in Section IV.

In summary, three key problems of robotic polishing are addressed in this article to achieve desired material removal depths on the complex workpiece surface, which are also contributions to the state of the art.

- 1) A numerical contact mechanics model is developed to predict the material removal depths on the complex workpiece surface. By representing the workpiece as the point cloud, analytical expressions of the workpiece surface can be avoided. The contact pressure distribution is calculated based on the nonlinear stress-strain law and the numerical point-surface distance. The material removal depths can be predicted on the workpiece point cloud efficiently.

- 2) A high-priority subregion searching algorithm is developed, which is very different from the existing surface partitioning methods. The Gaussian kernel function is utilized to locate the center point of the high-priority subregion. Thus, the tool is guided to polish those workpiece points with a large redundant material depth. Compared to the patch-based surface partitioning methods, the proposed algorithm is task-oriented (to achieve desired material removal) and easy to use, especially for the point-sampled workpiece surfaces.

- 3) A removal profile function is proposed to describe the shape feature of the removal profile after polishing along a straight path. It can be used to determine the initial path direction that covers the maximal volume of redundant materials. The tool dwell times along each path and the path spacings in the extracted subregion are planned sequentially to minimize the deviation from the desired material removal depths.

It should be mentioned that we do not pursue globally optimal trajectory solutions since the dimensionality of the path search space has already been reduced to generate practical and effective tool trajectories quickly. This standpoint was also made in the previous study for the robotic spray-painting process [5].

The rest of this article is organized as follows. Some relevant works are briefly discussed in Section II. The numerical contact mechanics and material removal model for the point-sampled complex surfaces is developed in Section III. Section IV introduces the concept of the high-priority subregion and the subregion searching algorithm. In Section V, the path direction is first determined for the direction-parallel paths in a subregion. Then, the optimization of the tool dwell times and the path spacings is presented. In Section VI, the effectiveness of the proposed tool trajectory planning method is verified by performing disk polishing simulations and experiments on different workpieces, including several simple surfaces and a wheel hub. This article is finally concluded in Section VII.

II. RELATED WORKS

A. Contact Mechanics and Material Removal Modeling

The contact mechanics models can be classed into the analytical contact models and the numerical contact models. A most well-known analytical contact model is the Hertzian model [11], [12]. It assumes that the contact pressure distribution is elliptic, and the normal contact force is nonlinearly correlated with the surface curvature and the maximum contact depth. In our previous research [13], we developed a semi-analytical contact mechanics model for the tilted-disk polishing process. The polishing disk was assumed as an array of vertical elastic springs inspired by the contact modeling of soft fingers [14]. We analyzed the influence of the tool tilt angle on the normal contact force. The contact force equation was derived in a power-law form similar to the Hertzian contact model. The material removal depths along the polishing path can also be predicted straightforwardly.

Although the analytical contact model is the most efficient way to obtain the contact pressure distribution, it does not apply to workpiece features with noncontinuous curvatures, for example, when the tool passes across the holes or feeds along the sharp edges of the workpiece. A good alternative in such cases is using the numerical contact model. Feng *et al.* [15] modeled the contact pressure distribution in the disk polishing process by using a numerical point-surface distance approach. Their method assumed the workpiece is a smooth B-spline surface with continuous curvatures. A contact pressure model based on the finite element method (FEM) was developed for the belt grinding process [16]. The material removal depths can be visualized on the point-sampled workpiece, but the FEM is not suitable for fast material removal prediction. To the best of our knowledge, no contact mechanics model was developed to predict the material removal depths on the workpiece point cloud quickly.

B. Surface Partitioning

Researchers had developed various surface partitioning methods according to different criteria [8]. Liu *et al.* [17] used the K -means clustering algorithm to partition the surface into patches with similar normal directions. Sheng *et al.* [18] partitioned the workpiece surface into multiple patches based on the surface topologies and surface normal directions. Each patch has a simple shape and topology. The normal change in each patch is small. Atkar *et al.* [19] proposed a hierarchical surface partitioning procedure. The surface is first segmented into approximately extruded patches based on the Gaussian curvature. Then, the surface is partitioned into topologically simple components with no holes based on the Morse function. They further developed a cell-merging algorithm to improve deposition uniformity by minimizing the cell boundary effects. Although they had verified their method on a few automotive surfaces, the partitioning methods based on the convex decomposition algorithms are hard to implement for workpieces with more complex shapes or topological structures. Besides, dividing the surface into patches without holes is not a necessary condition. In practice, the polishing tool can pass those holes that are small compared to the tool radius directly under force control.

Some region-based machining studies choose to partition the workpiece surfaces according to the task-specific criteria, such as the forming error distribution [20], posture-dependent robot stiffness [21], or local gouging avoidance [22]. It has been demonstrated that these surface partitioning methods can improve machining accuracy and efficiency.

C. Tool Trajectory Planning

Planning the tool trajectory in a single surface patch using the direction-parallel path pattern can be decomposed into three subproblems: determining the path direction, the path spacing, and the tool dwell time (the reciprocal of the tool feed velocity) along each path.

There is no common standard to define the optimal path direction. For example, researchers who focus on the maximum material removal volume may choose the path direction

along with the minimum surface principal curvature [23], while researchers who focus on the feeding motion stability may choose the path direction that has the largest tool lateral stiffness [21]. In the robotic spray-painting study [5], the path direction is selected to minimize the patch width (the sum of lengths of the longest orthogonal geodesics on either side of the initial path), thus minimizing the cycle time.

When the path direction is determined, the polishing paths are generated as the repeating offsets of the initial path. The path spacing can be optimized to reduce the fluctuation of the material removal depths leveraging the overlapping effect between adjacent polishing paths [2]. Based on the material removal model, Feng *et al.* [15] derived the analytical solution of the optimal path spacing for disk polishing of a planar workpiece. A numerical iteration method was developed by Han *et al.* [10] to determine the path spacing that achieves physically uniform coverage of an NURBS surface. A path spacing planning algorithm for belt polishing of a blade surface is established by Lv *et al.* [25]. The geometric derivation of the path spacing based on the constant chord-height error constraint is quite complicated. In the spray-painting planning studies, Chen and Xi [26] utilized the pattern search method to find the path spacing that minimizes the mean squared error of the deposition thicknesses between adjacent paths. Atkar *et al.* [5] searched the path spacing that minimizes an objective function consisting of the standard deviation of deposition thickness, surface altitude, and path spacing variation. These algorithms are all developed for the analytical surfaces.

As for the tool dwell time planning, Atkar *et al.* [5] used the speed parameterization approach to obtain the tool feed velocity that achieves uniform deposition thickness along a painting path. Huang *et al.* [27] planned the tool dwell times to minimize the deviation from the desired material removal depths. A constrained linear least-squares (CLLS) equation is solved considering the maximum and minimum tool feed velocities. In [27], the path spacings are predetermined, and the tool dwell times at all the sampled path points are optimized simultaneously. It is less efficient than planning the tool dwell times and the path spacing sequentially. Han *et al.* [24] presented an iterative compensation method to plan the tool dwell times that achieve the desired material removal depths along each polishing path. They adapted the path spacings in different workpiece regions and considered the dynamics constraints of the polishing tool in the tool dwell time optimization.

III. NUMERICAL CONTACT MECHANICS AND MATERIAL REMOVAL MODEL

In this research, the abrasive disk is chosen as the polishing tool, which has merits such as lightweight and high polishing efficiency [13]. It should be noted that this model can be generalized to other types of polishing tools, such as the spherical tool [12] or belt tool [25]. When the polishing disk presses on the workpiece with a tilt angle, it deforms and generates a contact area wherein the contact pressure is positive. The workpiece material in the contact area is removed by the abrasive grains adhered to the bottom surface

of the rotating disk. To simulate the material removal depths, the contact depth at each workpiece point is calculated first. Nonlinear stress-strain law is then used to predict the contact pressure. Finally, the Preston equation can be utilized to predict the material removal depth.

A. Numerical Contact Mechanics Model

The point cloud of a workpiece surface can be obtained from the CAD model or sampled by a high-accurate 3-D scanner. As shown in Fig. 2(a), the positions of the sampled workpiece points in the world frame $\{\mathbf{O}_W\}$ are denoted as

$$\mathbf{W}|_{\{\mathbf{O}_W\}} = \{\mathbf{W}_k\} = \{(x_k, y_k, z_k) | k = 1, \dots, N\} \quad (1)$$

where N is the number of sampled workpiece points. The point cloud can be up- or down-sampled according to the tradeoff between model accuracy and computational efficiency. For example, the point cloud of a wheel hub with a uniform sampling distance of 2 mm is displayed in Fig. 1.

As for the compliant polishing disk, its radius and height are denoted as R and H , respectively. To compute the normal contact force along the tool axis direction, imagine that the polishing disk is composed of an array of virtual springs that are perpendicular to the disk bottom surface. As plotted in Fig. 2(b), we choose to discretize the disk bottom surface based on the polar coordinates. Thus, the normal contact force F_N can be calculated as the weighted sum of all the contact pressures at the discretized disk points

$$F_N = \sum_{i=1}^I p_i \cdot \Delta S_i = E \cdot \sum_{i=1}^I (|h_i|/H)^\beta \cdot \Delta S_i \quad (2)$$

where I is the number of discretized disk points. $p_i = E \cdot (|h_i|/H)^\beta$ is the contact pressure at the i th disk point. It is computed based on a nonlinear stress-strain constitutive law [13]. Here, E is the nonlinear material modulus, and β is the stress-strain power index that can be identified through the tool loading tests. h_i is the contact depth at the i th disk point. ΔS_i represents the weighted area of the i th disk point, and it can be obtained as follows according to the polar coordinates:

$$\Delta S_i = r_i \cdot dr_i \cdot d\theta_i. \quad (3)$$

The remaining work is to determine the contact depth h_i at the i th disk point, i.e., the distance from the i th disk point to the workpiece surface along the tool axis direction. Note that the workpiece surface is embedded in an unstructured point cloud, and a plane function can be used to fit the workpiece points whose projections on the disk bottom surface are near the i th disk point. The contact depth h_i is obtained by computing the distance from the i th disk point to the locally fitted plane along the tool axis direction. For the negative contact depths, they are set to zero since they do not contribute to the normal contact force. With a given initial tool frame $\{\mathbf{O}_T\}$ and a given maximum contact depth h_0 , the contact depths at all the discretized disk points can be calculated.

The pseudocode of computing the normal contact force F_N based on (2) is provided in Algorithm 1. The loop from lines 4–9 accumulates the contact pressures at all the

Algorithm 1 Compute Normal Contact Force

Input: $\{\mathbf{O}_T\}, h_0$
Output: F_N

- 1: Translate the initial tool frame $\{\mathbf{O}_T\}$ along the tool axis direction a depth h_0 .
- 2: Describe the point cloud $\mathbf{W}|_{\{\mathbf{O}_T\}}$ in the current tool frame $\{\mathbf{O}_T\}$.
- 3: $F_N \leftarrow 0$
- 4: **for** $i = 1 : I$ **do**
- 5: $(x_i, y_i) \leftarrow$ the x, y coordinates of the i th disk point in the current tool frame $\{\mathbf{O}_T\}$.
- 6: Approximate the contact depth $\hat{z}(x_i, y_i)$ using plane fitting of the local workpiece points whose x, y coordinates are near (x_i, y_i) .
- 7: $h_i = \max(\hat{z}(x_i, y_i), 0)$;
- 8: $F_N \leftarrow F_N + E \cdot (h_i/H)^\beta \cdot \Delta S_i$;
- 9: **end for**
- 10: **return** F_N

discretized disk points to obtain the resultant normal contact force. Line 7 ensures that the contact depths are positive.

During the polishing process, the maximum contact depth h_0 cannot be controlled accurately since it cannot be measured by a displacement sensor directly. Instead, the normal contact force F_N can be controlled by using a pneumatic or motor-driven end-effector with the force-control functionality [28]. Suppose that the normal contact force is maintained as the nominal value F_N^d , and the maximum contact depth h_0 needs to be estimated inversely to calculate the contact pressures. As the normal contact force F_N is a monotone raising function of the maximum contact depth h_0 (see Algorithm 1), the secant method [30] can be utilized to solve the equation $F_N(\{\mathbf{O}_T\}, h_0) = F_N^d$. The pseudocode of estimating the maximum contact depth h_0 is given in Algorithm 2. Lines 1–3 compute the force estimation residues of the two test depths $h_{0(1)}$ and $h_{0(2)}$. The loop from lines 4 to 10 estimates the solution of h_0 iteratively until the force estimation residue is smaller than a threshold η .

Algorithm 2 Compute Maximum Contact Depth

Input: $\{\mathbf{O}_T\}, F_N^d$
Output: h_0

- 1: $h_{0(1)} \leftarrow 0, h_{0(2)} \leftarrow 2$ mm.
- 2: $Residue_1 \leftarrow F_N(\{\mathbf{O}_T\}, h_{0(1)}) - F_N^d$.
- 3: $Residue_2 \leftarrow F_N(\{\mathbf{O}_T\}, h_{0(2)}) - F_N^d$.
- 4: **while** $|Residue_2| \geq \eta$ **do**
- 5: $h_0 \leftarrow h_{0(2)}$
- 6: $h_{0(2)} \leftarrow h_{0(2)} - Residue_2 \cdot \left(\frac{Residue_2 - Residue_1}{h_{0(2)} - h_{0(1)}} \right)^{-1}$
- 7: $Residue_2 \leftarrow F_N(\{\mathbf{O}_T\}, h_{0(2)}) - F_N^d$.
- 8: $h_{0(1)} \leftarrow h_0$
- 9: $Residue_1 \leftarrow F_N(\{\mathbf{O}_T\}, h_{0(1)}) - F_N^d$.
- 10: **end while**
- 11: **return** h_0

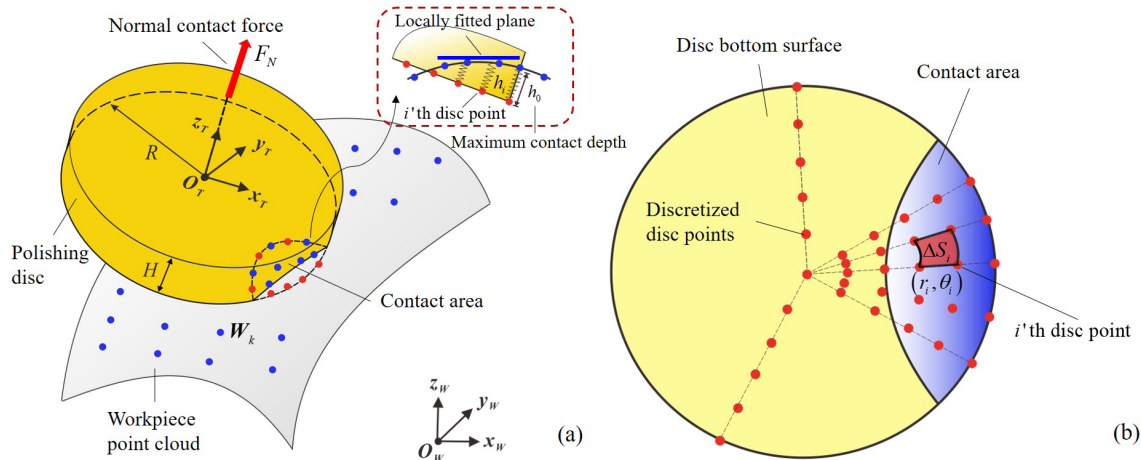


Fig. 2. (a) Compliant polishing disk and the workpiece surface point cloud (blue points). (b) Discretized disk points (red points) to calculate the resultant normal contact force under the maximum contact depth h_0 .

B. Numerical Material Removal Model

The material removal depth can be predicted by using the Preston equation [6]. In the Preston equation, the material removal rate (MRR) at a workpiece point is proportional to the contact pressure P and the tool sliding velocity v_s . The material removal depth then equals to the MRR times the tool dwell time

$$dh = k_p \cdot P \cdot v_s \cdot dt \quad (4)$$

where k_p is the experimentally identified material removal coefficient. For the MRR of the k^{th} workpiece point W_k , the contact pressure P_k and the tool sliding velocity $v_{s,k}$ on this point can be obtained as

$$\begin{cases} (P_k, v_{s,k}) = \left(E\left(\frac{z_k}{H}\right)^\beta, \omega(x_k^2 + y_k^2) \right) \\ \text{for } 0 \leq z_k \leq H \text{ and } x_k^2 + y_k^2 \leq R^2 \\ (P_k, v_{s,k}) = (0, 0) \text{ else} \end{cases} \quad (5)$$

where ω is the tool angular speed. For the convenience of writing, the coordinates (x_k, y_k, z_k) of the workpiece points have already been transformed into the current tool frame $\{\mathbf{O}_T\}$ with the maximum contact depth h_0 . If a workpiece point is not in contact with the disk bottom surface, its contact pressure and tool sliding velocity are both set as zero. Finally, the material removal profile can be obtained by calculating the material removal depths for all the workpiece points based on (4). An overall flowchart of the numerical contact mechanics and material removal model is given in Fig. 3.

C. Removal Profile Function

Now, we define the removal profile function $\Phi(x)$ to describe the shape feature of the removal profile in the disk polishing process. It should be noted that the removal profile is not constant when the workpiece curvature is varying. However, we can choose the shape of the removal profile that is most likely to happen. That is, the removal profile is chosen as the cross section of the removal volume when the polishing disk passes across a planar workpiece at a constant velocity, as can be seen in Fig. 4. According to our

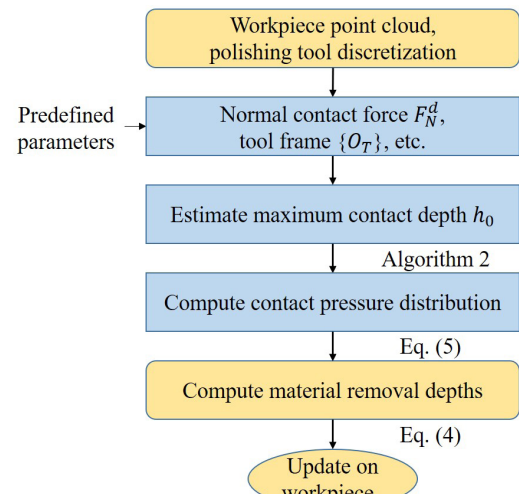


Fig. 3. Flowchart of the numerical contact mechanics and material removal model.

previous research [13], the removal profile function $\Phi(x)$ can be obtained as follows:

$$\Phi(x) = \begin{cases} \left(1 - \frac{x^2}{w^2}\right)^{\beta+1} & \text{for } |x| \leq w \\ 0 & \text{for } |x| > w \end{cases} \quad (6)$$

where w is half the polishing width and β is the stress-strain power index. w can be computed when the disk radius, disk tilt angle, and the normal contact force are given [13]. Note that, in (6), we have normalized the maximum material removal depth as 1. Therefore, $\Phi(x)$ is independent of the tool dwell time. For workpiece points on the polishing path, they have the maximum material removal depths, so we have $\Phi(0) = 1$. For workpiece points out of the polishing width, they are not been polished, so we have $\Phi(x) = 0$. The removal profile functions with different β values are plotted in Fig. 4.

IV. HIGH-PRIORITY SUBREGION SEARCHING

The proposed subregion searching algorithm is different from the existing surface partitioning methods [8], where

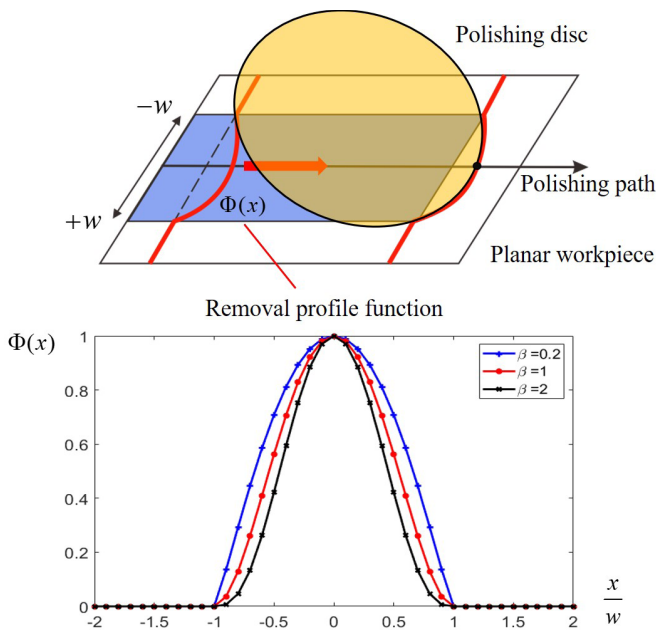


Fig. 4. Removal profile function $\Phi(x)$ with different β values. $\Phi(x)$ describes the shape feature of the removal profile in the disk polishing process.

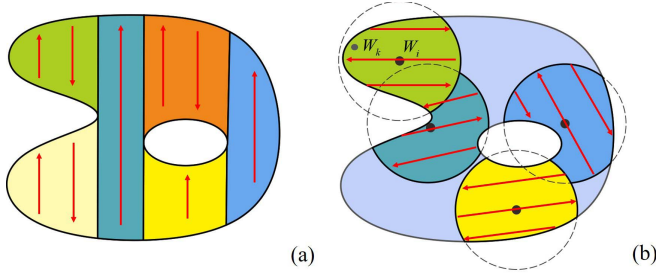


Fig. 5. Illustration of the surface partitioning methods based on (a) surface patches and (b) subregion defined in this article. Each subregion is a cluster of neighboring points with a center point.

nonoverlapping patches are partitioned in a single step and have strict borders between each other. In this study, relatively flat subregions are generated iteratively to track the most-worth-polishing workpiece points. To some degree, it can be viewed as a virtual online programming process since it needs feedback of the material removal depths after polishing in this subregion is finished. However, the update of the material removal depths is provided by the developed numerical material removal model, rather than measuring them via the real hardware. Therefore, it still belongs to the off-line programming methods.

A. Subregion Definition

First, we use the term ‘‘subregion’’ to differentiate from the term ‘‘patch’’ utilized in previous surface partitioning methods. As plotted in Fig. 5, ‘‘patch’’ is one piece of the surface divided by lines or curves, while ‘‘subregion’’ is a cluster of neighboring points with a center point. Specifically, the subregion is defined as the workpiece points from which the orientation weighted distances to the center point are

smaller than a radius R_I . For example, if the workpiece point W_i is the center point, its subregion can be expressed as

$$\text{Subregion}_i = \{W_k | \text{Dist}(W_i, W_k) \leq R_I\} \quad (7)$$

where we define the orientation weighted distance

$$\text{Dist}(W_i, W_k) = \|W_i - W_k\|_2 + w_o \cdot \text{acos}(\mathbf{n}_{W_i} \cdot \mathbf{n}_{W_k}) \quad (8)$$

where $\|\cdot\|_2$ is the Euclidean distance. In (8), \mathbf{n}_{W_k} represents the surface normal direction at the workpiece point W_k . w_o is the weight coefficient of the normal direction change relative to the point position change. The reason for defining an orientation-weighted distance is that a relatively flat subregion can be found near the selected center point. It avoids generating tool paths that cross the sharp edges. We do not make further convex decomposition for an extracted subregion since the convexity and topology have already been simplified compared to the global workpiece by choosing a relatively small subregion radius R_I . Although small holes or concave edges may appear in a subregion, these irregular features can be handled by performing a simple lift-and-drop tool motion or just being passed directly by the tool under force control, depending on the gap distances.

B. High-Priority Subregion Searching

To determine which subregion should be polished first, a human-like decision process is adopted here. It cannot be proved that such a solution is optimal, but it is indeed effective. First, let us consider that different rewards can be assigned on the workpiece points. In our polishing task, the reward is designed as the redundant material depth Re_k ($k = 1, \dots, N$), i.e., the depth of material that remained to be removed at a workpiece point. It is expected that the total rewards should be large in the extracted subregion. Hence, we define the subregion reward as the weighted sum of the rewards in the subregion, denoted as \bar{Re}_i ($i = 1, \dots, N$). The weight of each reward in the subregion is determined based on the Gaussian kernel function. The best advantage of using the Gaussian kernel function is that workpiece points with a large reward can be concentrated around the selected center point. The subregion reward \bar{Re}_i is defined as

$$\bar{Re}_i = \frac{1}{2\pi\sigma^2\rho^2} \sum_k Re_k \cdot e^{-\frac{\text{Dist}^2(W_i, W_k)}{2\sigma^2}} \quad \forall W_k \in \text{Subregion}_i \quad (9)$$

where σ is the standard deviation of the Gaussian kernel function. ρ is the sampling density of the workpiece point cloud. A suggested σ in our study is $0.5R_I$. It can be verified that, with this σ , the weights are relatively small for workpiece points on the subregion boundary ($\text{Dist}(W_i, W_k) = R_I$).

Another factor that needs to be considered is the machining efficiency. It is measured by moving the polishing tool to the center point W_i and aligning the tool axis \mathbf{n}_T along with the surface normal at W_i . Suppose that the tool frame is $\{\mathbf{O}_T\}$, and the tool-movement cost can be defined as follows:

$$\text{Dist}(\{\mathbf{O}_T\}, W_i) = \|\mathbf{O}_T - W_i\|_2 + w_o \cdot \text{acos}(\mathbf{n}_T \cdot \mathbf{n}_{W_i}) \quad (10)$$

where \mathbf{O}_T represents the position of the tool frame's origin, i.e., the disk center.

To determine the center point of the most-worth-polishing subregion, we now define the priority Prior_i at each workpiece point \mathbf{W}_i . The priority consists of two parts. The first part is the subregion reward $\overline{\text{Re}}_i$ obtained from (9), i.e., the weighted sum of the redundant material depths. The second part is the tool-movement cost $\text{Dist}(\{\mathbf{O}_T\}, \mathbf{W}_i)$ obtained from (10). Hence, Prior_i is defined as

$$\text{Prior}_i = \overline{\text{Re}}_i - w_m \cdot \text{Dist}(\{\mathbf{O}_T\}, \mathbf{W}_i) \quad (11)$$

where w_m is the weight coefficient of the tool-movement cost relative to the subregion reward. Based on (11), the optimal center point can be selected as the workpiece point with the highest priority

$$\text{CenterIndex}^* = \arg \max_i \text{Prior}_i, \quad i \in 1, 2, \dots, N \quad (12)$$

where CenterIndex^* denotes the point index of the optimal center point. Finally, the high-priority subregion can be extracted based on the center point index CenterIndex^* and the subregion radius R_I , given as follows:

$$\begin{aligned} \text{Subregion}^* = \{ & \mathbf{W}_k | \text{Dist}(\mathbf{W}_{\text{CenterIndex}^*}, \mathbf{W}_k) \leq R_I, \\ & k \in 1, 2, \dots, N \}. \end{aligned} \quad (13)$$

As for selecting the hyperparameter R_I , a too large or too small R_I is not appropriate. For example, if R_I is set very large, the generated subregion may contain many complex features. The normal direction change in the subregion may also be large. If R_I is set very small, there will be too many subregions generated, bringing side effects, such as frequent tool returns and unexpected overlaps between subregions. Neither of these situations is beneficial for polishing path planning. Besides, for workpieces with a different size or shape, the best R_I may change. In this article, we compare the simulation results of using different subregion radii R_I (see Section VI-B) and then select the R_I with the best performance both in accuracy and efficiency.

V. LOCAL TRAJECTORY PLANNING

A. Path Direction Planning

We have known in Section IV that the lack-polished workpiece points are concentrated around the center point of the extracted high-priority subregion. Then, a natural way to plan the initial path is to let it pass the subregion center point and have the direction covering the maximal volume of redundant materials. Therefore, the subregion reward $\overline{\text{Re}}$ can be decreased to the maximum extent after polishing along this initial path.

We use the example of a rectangular workpiece with a nonuniform redundant material distribution to explain the characteristic of our path-direction planning method compared with that developed in [5]. The comparison of the two initial path directions is shown in Fig. 6. For the path direction planned by the method developed in [5], the polishing path is parallel to the longer side of the workpiece. However, this path direction is inefficient for the nonuniform redundant

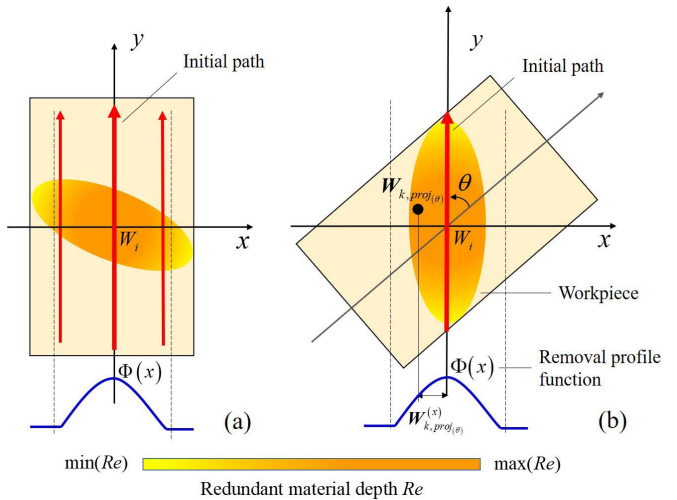


Fig. 6. Rectangular workpiece with the path direction planned by (a) method developed in [5] and (b) our proposed method. In (b), the initial path covers the largest volume of redundant materials. The orange area represents the workpiece points with a large redundant material depth.

material distribution presented in our example, as multiple paths should be generated to cover the orange area (points with large redundant material depths). In comparison, our planning method requires fewer paths to cover the orange area.

A mathematical definition of the optimal path direction is given as follows. The previously developed removal profile function $\Phi(x)$ [see (6)] is served as a “1-D convolution kernel” to evaluate how much redundant materials can be removed after polishing along the initial path. Let the path direction angle denoted as θ , the optimal path direction angle θ^* can be obtained as

$$\theta^* = \arg \max_{\theta} \sum_k \text{Re}_k \cdot \Phi(W_{k,\text{proj}(\theta)}^{(x)}) \quad \forall W_k \in \text{Subregion} \quad (14)$$

where $W_{k,\text{proj}(\theta)}^{(x)}$ denotes the x component of the workpiece point W_k that is projected on the tangent plane of the center point. The coordinate system of the tangent plane has already rotated an angle θ , as plotted in Fig. 6(b).

B. Tool Dwell Time Planning

We choose to plan the tool dwell time and the path spacing sequentially to reduce the number of optimizable variables. The coordinate system of the extracted subregion is called the local frame, with the origin located at the subregion center point. Without loss of generality, the y -axis of the local frame can be set as parallel to the planned path direction. As shown in Fig. 7, the locations of the polishing paths from left to right are denoted as $x = x_n$, $n = 1, 2, \dots$. The lower and upper limits of the path $x = x_n$ are given by y_n^L and y_n^U , respectively. Each polishing path is sampled from up to down with a uniform sampling interval δ . Thus, the projections of the sampled path points $Q_j^n (j = 1, \dots, \lfloor ((y_n^U - y_n^L)/\delta) \rfloor)$ on the local frame's xy plane are given as

$$Q_{j,\text{proj}}^n = (x_n, y_n^U - (j-1)\delta), \quad j = 1, \dots, \left\lfloor \frac{y_n^U - y_n^L}{\delta} \right\rfloor \quad (15)$$

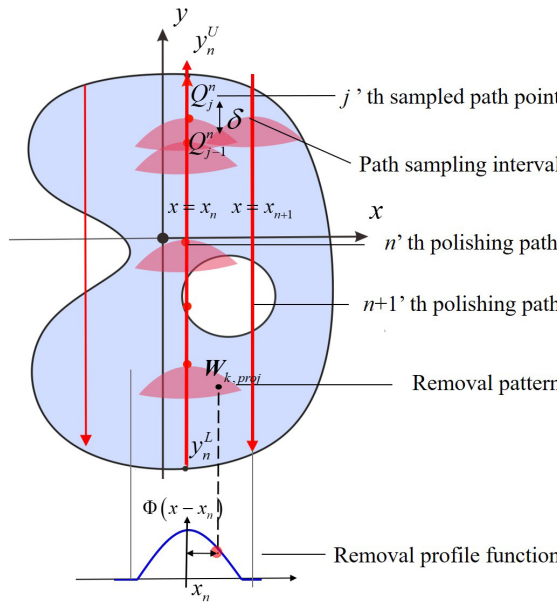


Fig. 7. Direction-parallel polishing paths (red lines) and the sampled path points. The polishing tool affects the material removal depths of nearby workpiece points in various degrees, which are described by the defined removal profile function $\Phi(x)$.

where $\lfloor \cdot \rfloor$ is the round-down operation. The subscript proj denotes a point's projection on the local frame's xy plane. It is assumed that the tool axis lies in the same plane spanned by the path direction and the workpiece normal $\mathbf{n}_{Q_j^n}$ at Q_j^n . Hence, for each sampled path point Q_j^n , the tool frame $\{\mathbf{O}_T\}|_{Q_j^n}$ can be calculated as

$$\{\mathbf{O}_T\}|_{Q_j^n} = \begin{bmatrix} \mathbf{f} \times \mathbf{n}_{Q_j^n} & \mathbf{n}_{Q_j^n} \times (\mathbf{f} \times \mathbf{n}_{Q_j^n}) & \mathbf{n}_{Q_j^n} & Q_j^n \\ 0 & 0 & 0 & 1 \end{bmatrix} \cdot \begin{bmatrix} 1 & 0 & 0 & 0 \\ 0 & \cos\theta & \sin\theta & 0 \\ 0 & -\sin\theta & \cos\theta & 0 \\ 0 & 0 & 0 & 1 \end{bmatrix} \cdot \begin{bmatrix} 1 & 0 & 0 & 0 \\ 0 & 1 & 0 & -R \\ 0 & 0 & 1 & 0 \\ 0 & 0 & 0 & 1 \end{bmatrix} \quad (16)$$

where \mathbf{f} denotes the path direction given in the world frame and θ is the disk tilt angle. The maximum contact depth h_0 at Q_j^n can be calculated based on Algorithm 2 with the known tool frame $\{\mathbf{O}_T\}|_{Q_j^n}$ and the nominal normal contact force F_N^d .

Let \mathbf{MR}^n denote the material removal matrix of the extracted subregion when the polishing path is along $x = x_n$. The element MR_{ij}^n of \mathbf{MR}^n is given by the MRR at the i th subregion point when the tool locates at the j th sampled path point. From Section III, we have already known how to compute the MRR. Thus, suppose that the tool dwell times along path $x = x_n$ are given by $\mathbf{T}^n = (t_1^n, \dots, t_{|\mathcal{Q}^n|}^n)^T$ ($|\mathcal{Q}^n|$ is the number of sampled path points), and the material removal depths in the extracted subregion can be calculated as $\mathbf{MR}^n \cdot \mathbf{T}^n$.

The goal of planning the tool dwell times along the path $x = x_n$ is to reduce the deviation from the desired material removal depths. Note that the tool affects the material removal depths of nearby workpiece points in various degrees, which are described by the removal profile function (6). Hence, we discount the desired material removal depths of the

workpiece points near $x = x_n$ by $\Phi(x - x_n)$. The optimization of the tool dwell times \mathbf{T}^n along $x = x_n$ can be handled as a CLLS problem as follows:

$$\begin{aligned} \mathbf{T}^{n*} = \arg \min_{\mathbf{T}^n} & \| \mathbf{MR}^n \cdot \mathbf{T}^n - \text{Re} \cdot \Phi(\mathbf{W}_{\text{proj}}^{(x)} - x_n) \|_2 \\ \text{s.t. } & t_{\min} \leq \mathbf{T}^n \leq t_{\max} \end{aligned} \quad (17)$$

where Re denotes all the redundant material depths in the subregion. $\mathbf{W}_{\text{proj}}^{(x)}$ denotes the x components of all the subregion points described in the local frame. t_{\min} and t_{\max} are the reciprocals of the upper and lower limits of the tool feed velocities, i.e., $1/v_{f,\max}$ and $1/v_{f,\min}$. The tool feed velocities at the sampled path points can be simply obtained as $v_{f_i}^n = \delta/t_i^n$, $i = 1, \dots, |\mathcal{Q}^n|$. According to [27], a time differential term $\nabla \cdot \mathbf{T}^n$ can be added to the cost function by multiplying a weight coefficient w_t . It can be used to prevent large fluctuations of the adjacent tool dwell times

$$\begin{aligned} \mathbf{T}^{n*} = \arg \min_{\mathbf{T}^n} & \| \mathbf{MR}^n \cdot \mathbf{T}^n - \text{Re} \cdot \Phi(\mathbf{W}_{\text{proj}}^{(x)} - x_n) \|_2 \\ & + w_t \nabla \cdot \mathbf{T}^n \\ \text{s.t. } & t_{\min} \leq \mathbf{T}^n \leq t_{\max} \end{aligned} \quad (18)$$

where

$$\nabla = \begin{bmatrix} 1 & -1 \\ 1 & -1 \\ \vdots \\ 1 & -1 \end{bmatrix}.$$

The CLLS problem can be solved very quickly by utilizing the projection gradient methods. In this article, we employ the lsqslin function in MATLAB's optimization toolbox to solve problem (17) or (18).

C. Path Spacing Planning

Now, suppose that the n th polishing path is known as $x = x_n$. The redundant material depths in the subregion before and after polishing along the next path $x = x_{n+1}$ are given by $\text{Re}_{(n)}$ and $\text{Re}_{(n+1)}$, respectively. If the tool moves from the left-hand side to the right-hand side of the subregion, the next polishing path $x = x_{n+1}$ must satisfy $x_{n+1} > x_n$ (or $x_{n+1} < x_n$, if the tool moves from the right-hand side to the left-hand side). Our goal is to find the next optimal path location x_{n+1}^* (or the optimal path spacing $x_{n+1}^* - x_n$) that minimizes the mean squared error of the redundant material depths $\text{Re}_{(n+1),k}$ between the adjacent paths x_n and x_{n+1}

$$\begin{aligned} x_{n+1}^* = \arg \min_{x_{n+1}} & L \\ L = \text{mean} \left(\sum_k \text{Re}_{(n+1),k}^2 \right), & \forall \mathbf{W}_{k,\text{proj}}^{(x)} \in [x_n, x_{n+1}] \end{aligned} \quad (19)$$

where $\text{mean}(\cdot)$ is the mean function.

To find the next optimal path location x_{n+1}^* , the tool dwell times \mathbf{T}^{n+1} along the new path $x = x_{n+1}$ to predict $\text{Re}_{(n+1)}$ should be calculated based on (18) using the previous redundant material depths $\text{Re}_{(n-1)}$, instead of using $\text{Re}_{(n)}$. This is because, if $\text{Re}_{(n)}$ is used to obtain \mathbf{T}^{n+1} now, the local minimum of the cost function L can be reached by choosing

a very small path spacing $x_{n+1} - x_n$ and very short tool dwell times T^{n+1} . This can result in an inefficient new path that is very close to the previous one. In contrast, if $Re_{(n-1)}$ is used to obtain T^{n+1} , the new path spacing will not be too large or too small, and thus, the resultant tool dwell times will be more reasonable. Besides, if $Re_{(n-1)}$ is used to plan x_{n+1} , the cost function L in (19) can be treated as a single peak function with one minimum point. Hence, the golden section method [30] can be utilized to find the optimal solution of x_{n+1}^* efficiently. The pseudocode of searching the next optimal path location x_{n+1}^* is provided in Algorithm 3. Lines 1–4 calculate the cost function values of the two initial test path locations. The loop from lines 5 to 13 estimates the minimum point of the single-peaked cost function L using the golden section method until the difference between the test path locations is smaller than a threshold γ .

Algorithm 3 Find Next Optimal Path Location

Input: x_n , $Re_{(n-1)}$, $Re_{(n)}$

Output: x_{n+1}^*

```

1:  $\alpha \leftarrow 0.618$ .
2:  $a \leftarrow x_n$ ,  $b \leftarrow x_n + 100$ ,
    $\lambda \leftarrow a + (1 - \alpha)(b-a)$ ,  $\mu \leftarrow a + \alpha(b-a)$ 
3: Calculate  $Re_{(n+1)-1}$  and  $Re_{(n+1)-2}$  for the two test polishing paths  $x = \lambda$  and  $x = \mu$ . The tool dwell times are solved based on (18) using  $Re_{(n-1)}$ .
4: Calculate the cost functions of the test path locations:
    $L_1 = \text{mean}(\sum_k Re_{(n+1),k}^2)$ ,  $\forall W_{k,\text{proj}}^{(x)} \in [x_n, \lambda]$ 
    $L_2 = \text{mean}(\sum_k Re_{(n+1),k}^2)$ ,  $\forall W_{k,\text{proj}}^{(x)} \in [x_n, \mu]$ 
5: while  $|a - b| \geq \gamma$  do
6:   if  $L_1 \geq L_2$  then
7:      $a \leftarrow \lambda$ ,  $\lambda \leftarrow \mu$ ,  $\mu \leftarrow a + \alpha(b-a)$ ,  $L_1 = L_2$ 
8:     Update cost function  $L_2$ 
9:   else
10:     $b \leftarrow \mu$ ,  $\mu \leftarrow \lambda$ ,  $\lambda \leftarrow a + (1 - \alpha)(b-a)$ ,  $L_2 = L_1$ 
11:    Update cost function  $L_1$ 
12:  end if
13: end while
14:  $x_{n+1}^* = (a + b)/2$ 
15: return  $x_{n+1}^*$ 
  
```

After the new path location x_{n+1} is determined, the tool dwell times T^{n+1*} along $x = x_{n+1}$ are now calculated based on (18) using the current redundant material depths $Re_{(n)}$. The material removal depths in the extracted subregion are updated, and the next polishing path $x = x_{n+2}$ can be found in the same way by implementing Algorithm 3. It should be noted that the polishing paths in the subregion are planned on the left- and right-hand sides of the initial path $x = 0$ separately. Thus, the generation of the new polishing path continues until the new path reaches the left or right limit of the subregion.

When the local trajectory planning procedure completes, the maximum subregion reward $\max(\bar{Re})$ on the global workpiece has decreased, and the new high-priority subregion can be found based on (12). Then, the local trajectory planning procedure is performed for the new subregion again. This finding of the new high-priority subregion terminates until the

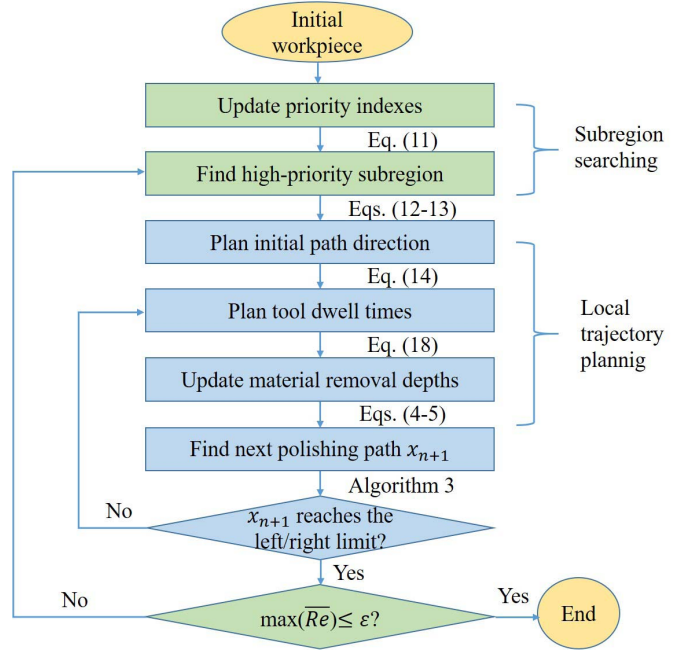


Fig. 8. Flowchart of the high-priority subregion searching and local trajectory planning algorithm.

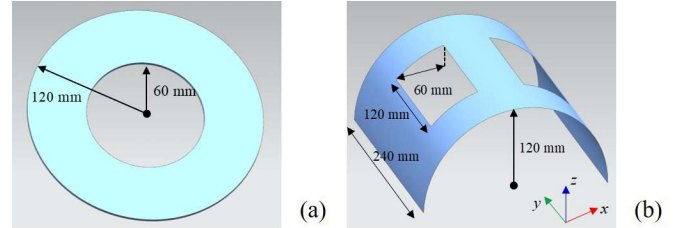


Fig. 9. (a) Ring-like surface and (b) grooved cylindrical surface.

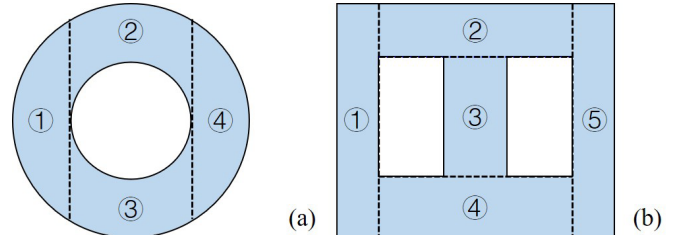


Fig. 10. Surface partitions of (a) ring-like surface and (b) grooved cylindrical surface. The numbers indicate different partitioned patches.

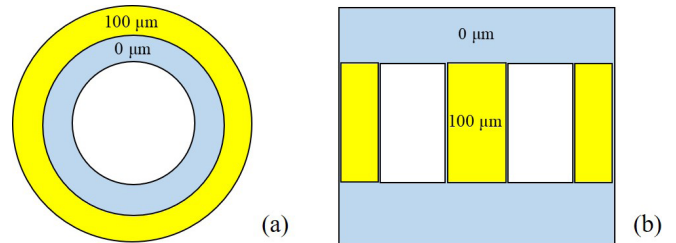


Fig. 11. Initial redundant material depths on (a) ring-like surface and (b) grooved cylindrical surface.

maximum subregion reward, $\max(\bar{Re})$, is smaller than a target value ε , which allows a small volume of redundant materials that may not be perfectly removed on the final workpiece.

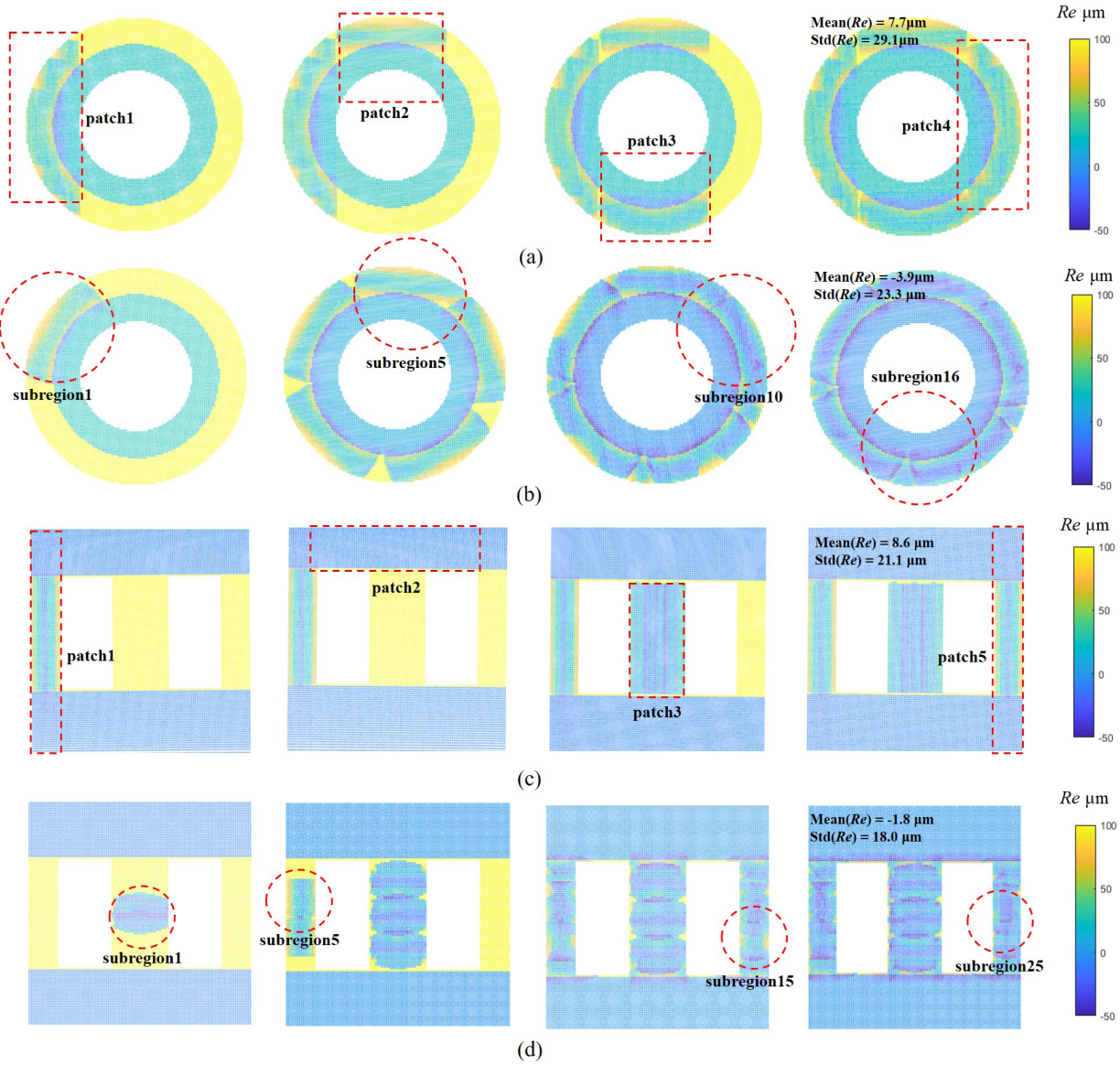


Fig. 12. Update processes of the redundant material depths on (a) ring-like surface using the patch-based method, (b) ring-like surface using the proposed method, (c) grooved cylindrical surface using the patch-based method, and (d) grooved cylindrical surface using the proposed method.

The flowchart of the high-priority subregion searching and local trajectory planning algorithm is given in Fig. 8.

VI. SIMULATION AND EXPERIMENT

To test the effectiveness of the proposed tool trajectory planning method for workpieces with different shapes, numerical polishing simulations are conducted on several simple analytical surfaces and a complex wheel hub surface. Then, a polishing experiment is carried out on an actual wheel hub surface using the tool trajectories generated in simulation.

For all the numerical simulations, we use the experimentally identified material properties and the predefined process parameters, as given in Table I. The material properties include the nonlinear modulus E , the stress-strain power index β , and the material removal coefficient k_p . The process parameters include the disk tilt angle θ , the tool angular speed ω , and

TABLE I
MATERIAL PROPERTIES AND PREDEFINED PROCESS PARAMETERS

Disc radius R	40 mm
Disc height H	10 mm
Nonlinear modulus E	0.84 MPa
Stress-strain power index β	0.89
Material removal coefficient k_p	$2.8 \times 10^{-5} \text{ MPa}^{-1}$
Disc tilt angle θ	12°
Tool angular speed ω	5000 rpm
Normal contact force F_N^d	12 N

the nominal normal contact force F_N^d . The nominal polishing width w in (6) can be calculated as 20 mm [13].

For the high-priority subregion searching, w_o in (8) that weighs the surface normal change relative to the point position change is selected as 200, and w_m in (11) that weighs the

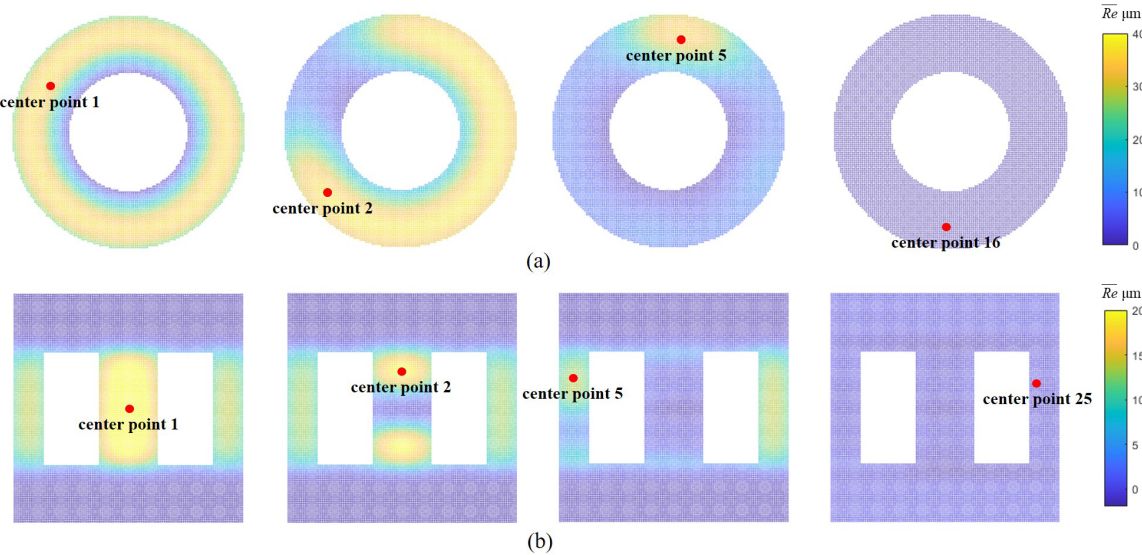


Fig. 13. Update processes of the subregion rewards $\bar{R}e$ and the subregion center points on (a) ring-like surface and (b) grooved cylindrical surface.

tool-movement cost relative to the subregion reward $\bar{R}e$ is set as $w_m = 0.001 \cdot \max(\bar{R}e)$. To obtain the tool dwell times along each path with a high resolution, the path sampling interval δ is set as 1 mm. The lower and upper bounds of the tool dwell times are $t_{\min} = 0.02$ s and $t_{\max} = 1$ s, and thus, the tool feed velocity cannot be larger or smaller than 50 or 1 mm/s, respectively. The weight coefficient w_t of the time fluctuation term in (18) is selected as 150. For a better force-control polishing performance, a planned polishing path is discarded if it is shorter than 20 mm. The tool also performs a simple lift-and-drop motion when it transfers to another path or passes across a gap that is wider than 20 mm.

The simulations are run on a desktop with an Intel Core i7-8700 CPU at 3.2-GHz 16-GB memory. The algorithms and the material removal rendering are performed in MATLAB 2020.

A. Polishing Simulation on Simple Surfaces

Two workpiece surfaces with relatively simple shapes are tested at first to compare the proposed high-priority subregion searching method with the patch-based surface partitioning method [19]. As shown in Fig. 9, the two surfaces include a ring-like surface and a grooved cylindrical surface. The patch-based surface partitions are provided in Fig. 10. It can be seen that multiple patches are generated to cover each surface.

The initial redundant material depths $R_{e(0)}$ on the workpiece are user-defined values, which are typically set as the initial surface form errors. We assume a nonuniform distribution of $R_{e(0)}$ on each workpiece, which can be observed in Fig. 11. The yellow areas indicate the positive redundant material depths (set as 100 μm in our example). In the implementation of the subregion searching algorithm, the subregion radius R_I is selected as 60 mm. The polishing disk starts at $[0, 0, 200]$ mm with the tool axis aligned with $[0, 0, 1]$. The target value ε of the maximum subregion reward $\bar{R}e$ is given by a fiftieth of its initial value, i.e., $\varepsilon = \max(\bar{R}e_{(0)})/50$.

In each divided patch or subregion, we use the proposed local trajectory planning algorithm to plan the tool dwell times and path spacings. The update processes of the redundant material depths on the two workpieces are visualized in Fig. 12. There are 16 subregions generated for the ring-like surface and 25 subregions generated for the grooved cylindrical surface to complete the polishing process. The material removal results show that both methods can remove the redundant materials to a desirable level, and only a small part of the surface is over or lack polished. Compared to the patch-based surface partitioning method, the proposed method yields a smaller mean value and a smaller standard deviation of the final redundant material depths. This is because, in the patch-based method, each patch is polished only once. Some areas are not sufficiently polished due to the inherent nature of the disk shape and the direction-parallel path pattern. Our proposed method provides a fine finishing of these lack-polished areas. However, it tends to slightly over polish the workpiece, as some areas are polished more than once.

We also visualize the update processes of the subregion rewards $\bar{R}e$ and the subregion center points in Fig. 13. It can be seen that the high-priority subregion can always track the brightest area (with the largest reward) on the workpiece surface. In the last step, there is no obvious positive subregion reward. Hence, the high-priority subregion searching process is terminated. The authors believe that this process is similar to the visual attention mechanism of humans.

B. Polishing Simulation on Wheel Hub

The top view of the tested wheel hub is shown in Fig. 15. It has a large mounting hole at its center, around which there are many screw holes, and radial spokes connecting the wheel's outer rim. For such a complex workpiece, we show that the proposed tool trajectory planning method is still competent.

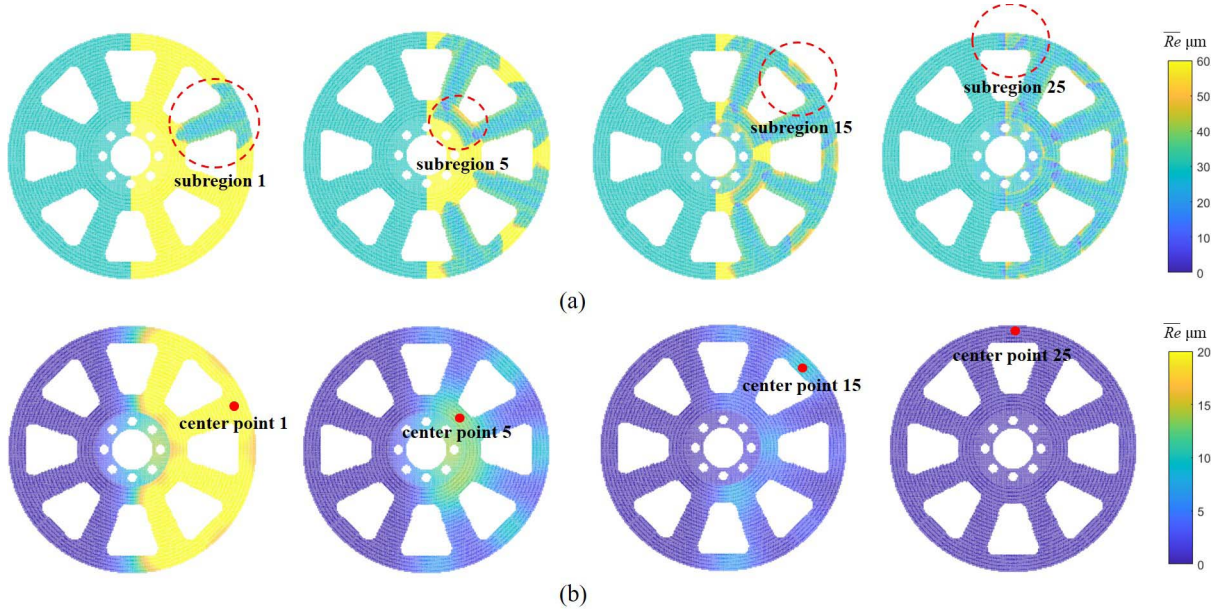


Fig. 14. Updates of (a) redundant material depths and (b) subregion rewards on the wheel hub using subregion radius $R_I = 80$ mm.

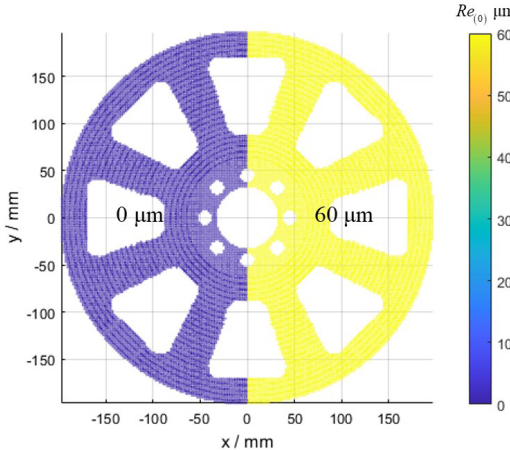


Fig. 15. Initial redundant material depths $Re_{(0)}$. $Re_{(0)}$ on the left- and right-hand sides of the wheel hub are set as 0 and 60 μm , respectively.

As shown in Fig. 15, the initial redundant material depths $Re_{(0)}$ on the left- and right-hand sides of the wheel hub in this example are defined as 0 and 60 μm , respectively. The implementation details of the proposed algorithms are the same as in Section VI-A, except that we now test four subregion radii $R_I = 40, 60, 80$, and 100 mm.

The absolute means, the standard deviations of the final redundant material depths, and the time consumptions of the polishing process using different subregion radii are compared in Fig. 16. It can be seen that $R_I = 80$ could acquire the optimal polishing performance both in accuracy and efficiency. Therefore, it can be later used to generate the tool trajectories in the wheel hub polishing experiment. The update processes of the redundant material depths and the subregion rewards on the wheel hub are visualized in Fig. 14. Almost all the redundant materials can be well removed after 25 high-priority subregions are generated.

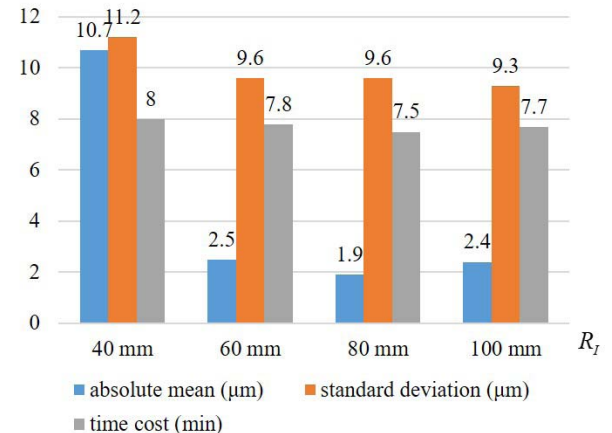


Fig. 16. Absolute means, the standard deviations of the final redundant material depths, and the time consumptions of the polishing process using different subregion radii.

The algorithm takes an average of 1 min to obtain the optimal path locations and tool dwell times in an extracted subregion. The overall computational time is about 30 min. We observed that the computational burden is mainly due to calculating the material removal matrices for all the sampled points along each path, which requires repeated estimation of the maximum contact depth based on Algorithm 2. A promising way to reduce the computational time is to leverage the parallel computing technique to compute the material removal matrices for all the sampled path points simultaneously.

C. Robotic Polishing Experiment

The ABB IR4400 robot with the force-control module is used to carry out the wheel hub polishing experiment. The experimental system is shown in Fig. 17. The motorized spindle can provide a constant tool rotating speed when the

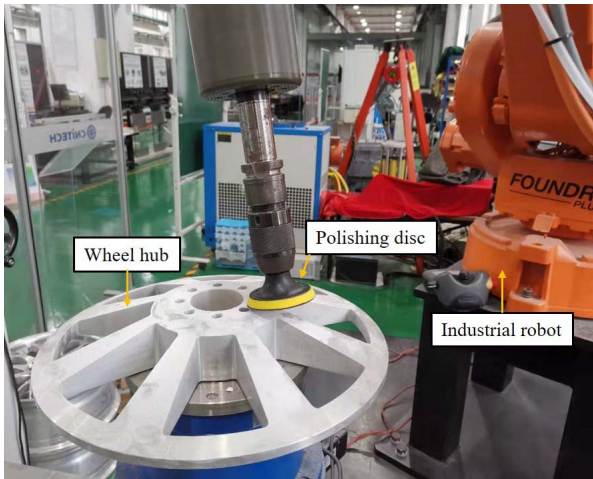


Fig. 17. Robotic polishing system and the wheel hub.

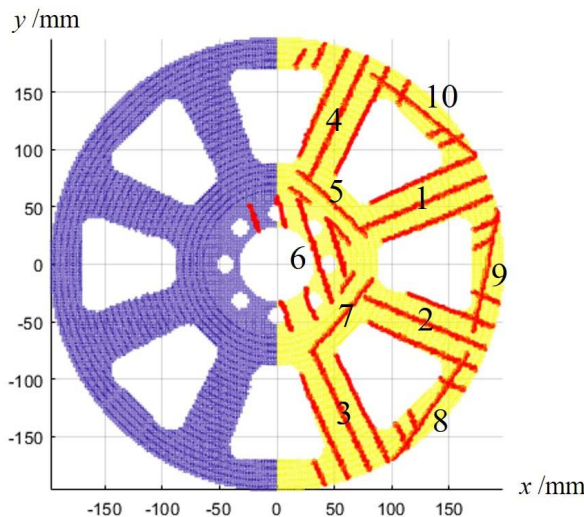
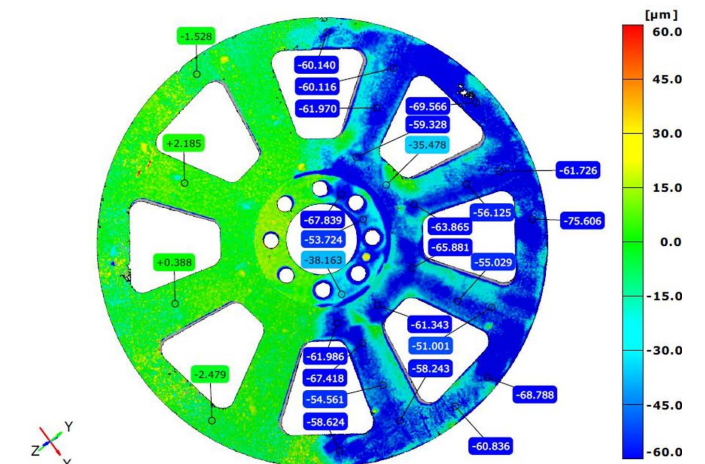


Fig. 18. Planned polishing paths (red lines) of the first ten high-priority subregions on wheel hub. Numbers 1–10 indicate the polishing sequence of those subregions.

normal contact force is varying. Before polishing, the wheel hub is measured by a high-accurate 3-D scanner ATOS-III, which can provide the point cloud data of the unpolished wheel hub's upper surface in a high resolution. In the robotic polishing experiment, the wheel hub is fixed on the testbed, and the workpiece frame relative to the robot base frame is precalibrated. The tool trajectories generated in the previous wheel-hub polishing simulation are written into the robot motion G-code. The industrial robot interpolates the adjacent tool locations automatically. Fig. 18 plots the planned polishing paths in the first ten high-priority subregions generated on the wheel hub surface.

After the polishing process is completed, the wheel hub is measured by the 3-D scanner again. The point cloud of the polished wheel hub's upper surface is projected onto the unpolished one (this operation is accomplished in the scanner's postprocessing software). The material removal depths can be approximated as the point-surface projection distances, as shown in Fig. 19. It can be observed that the average material removal depth on the right-hand side of the wheel hub has reached the desired 60 μm . Despite the lack-

Fig. 19. Material removal depths (measured by the 3-D scanner) on the wheel hub's upper surface. A uniform material removal depth of 60 μm has been achieved on the right-hand side of the wheel hub.

over-polished phenomenon due to the limitations of the robot force-control performance and the material removal model accuracy, the experimental result shows similar behaviors compared to the numerical simulation results [see Fig. 14(a)]. Therefore, the effectiveness of the proposed tool trajectory planning method has been verified.

VII. CONCLUSION

In this article, a tool trajectory planning method is developed to achieve the desired material removal depths on the point-sampled workpiece surface based on the numerical contact mechanics and material removal model. Under the nominal normal contact force, the maximum contact depth between tool and workpiece is estimated by using the secant method. The contact pressure distribution can be calculated efficiently based on nonlinear stress-strain law. Planning the tool trajectory on the global workpiece is simplified by generating tool paths in extracted subregions using the direction-parallel path pattern. The concept of the high-priority subregion is developed considering both subregion reward and tool-movement cost. As a result, the workpiece points with large redundant material depths can always be first polished. In each subregion, the planned path direction enables the initial path to cover the maximal volume of redundant materials. The tool dwell times along each path are optimized by solving a constraint linear least-squares problem, and thus, the deviation from the desired material removal depths near each path is minimized. The optimal path spacing is found by using the golden section method, and thus, the mean squared error of the redundant material depths between adjacent paths is minimized.

The simulation and experimental results show that the desired material removal depths can be achieved on the ring-like surface, the grooved cylindrical surface, and the wheel hub surface. Thus, the proposed method demonstrates good flexibility for workpieces with different shapes. Furthermore, the proposed method obtains a smaller mean value and smaller standard deviation of the final redundant material depths compared with the existing patch-based surface partitioning methods. Therefore, the proposed method could also achieve a higher polishing accuracy.

Our research is now focused on material removal since it can be modeled analytically. However, other analytical or statistical process models can be integrated into the proposed tool trajectory planning method. The future work will consider the roughness model that can help achieve the mirror finishing of a workpiece surface.

REFERENCES

- [1] D. Zhu *et al.*, "Robotic grinding of complex components: A step towards efficient and intelligent machining—Challenges, solutions, and applications," *Robot. Comput. Integrat. Manuf.*, vol. 65, Oct. 2020, Art. no. 101908.
- [2] J. J. Márquez, J. M. Pérez, J. Ríos, and A. Vizán, "Process modeling for robotic polishing," *J. Mater. Process. Technol.*, vol. 159, no. 1, pp. 69–82, 2005.
- [3] W.-L. Li, H. Xie, G. Zhang, S.-J. Yan, and Z.-P. Yin, "3-D shape matching of a blade surface in robotic grinding applications," *IEEE/ASME Trans. Mechatronics*, vol. 21, no. 5, pp. 2294–2306, Oct. 2016.
- [4] D. C. Conner, A. Greenfield, P. N. Atkar, A. A. Rizzi, and H. Choset, "Paint deposition modeling for trajectory planning on automotive surfaces," *IEEE Trans. Autom. Sci. Eng.*, vol. 2, no. 4, pp. 381–391, Oct. 2005.
- [5] P. N. Atkar, A. Greenfield, D. C. Conner, H. Choset, and A. A. Rizzi, "Uniform coverage of automotive surface patches," *Int. J. Robot. Res.*, vol. 24, no. 11, pp. 883–898, 2005.
- [6] F. W. Preston, "The theory and design of plate glass polishing machines," *J. Glass Technol.*, vol. 11, no. 44, pp. 214–256, 1927.
- [7] M. J. Tsai, J.-L. Chang, and J.-F. Haung, "Development of an automatic mold polishing system," *IEEE Trans. Autom. Sci. Eng.*, vol. 2, no. 4, pp. 393–397, Oct. 2005.
- [8] E. Galceran and M. Carreras, "A survey on coverage path planning for robotics," *Robot. Auto. Syst.*, vol. 61, no. 12, pp. 1258–1276, Dec. 2013.
- [9] W. H. Huang, "Optimal line-sweep-based decompositions for coverage algorithms," in *Proc. IEEE Int. Conf. Robot. Autom. (ICRA)*, May 2001, pp. 27–32.
- [10] Y. Han, L. Zhang, M. Guo, C. Fan, and F. Liang, "Tool paths generation strategy for polishing of freeform surface with physically uniform coverage," *Int. J. Adv. Manuf. Technol.*, vol. 95, nos. 5–8, pp. 2125–2144, Mar. 2018.
- [11] K. L. Johnson, *Contact Mechanics*. Cambridge, U.K.: Cambridge Univ. Press, 1985.
- [12] M. Rososhansky and F. Xi, "Coverage based tool-path planning for automated polishing using contact mechanics theory," *J. Manuf. Syst.*, vol. 30, no. 3, pp. 144–153, Aug. 2011.
- [13] M. Xiao, Y. Ding, Z. Fang, and G. Yang, "Contact force modeling and analysis for robotic disc polishing on freeform workpieces," *Precis. Eng.*, vol. 66, no. 65, pp. 614–624, 2020.
- [14] I. Kao and F. Yang, "Stiffness and contact mechanics for soft fingers in grasping and manipulation," *IEEE Trans. Robot. Autom.*, vol. 20, no. 1, pp. 132–135, Feb. 2004.
- [15] D. Feng, Y. Sun, and H. Du, "Investigations on the automatic precision polishing of curved surfaces using a five-axis machining centre," *Int. J. Adv. Manuf. Technol.*, vol. 72, nos. 9–12, pp. 1625–1637, Jun. 2014.
- [16] X. Ren, M. Cabaravdic, X. Zhang, and B. Kuhlenkötter, "A local process model for simulation of robotic belt grinding," *Int. J. Mach. Tools Manuf.*, vol. 47, no. 6, pp. 962–970, May 2007.
- [17] X. Liu, Y. Li, and Q. Li, "A region-based 3 + 2-axis machining toolpath generation method for freeform surface," *Int. J. Adv. Manuf. Technol.*, vol. 97, nos. 1–4, pp. 1149–1163, Jul. 2018.
- [18] W. Sheng, H. Chen, N. Xi, J. Tan, and Y. Chen, "Optimal tool path planning for compound surfaces in spray forming processes," in *Proc. IEEE Int. Conf. Robot. Autom. (ICRA)*, Apr. 2004, pp. 45–50.
- [19] P. N. Atkar, D. C. Conner, A. Greenfield, H. Choset, and A. A. Rizzi, "Hierarchical segmentation of piecewise pseudoextruded surfaces for uniform coverage," *IEEE Trans. Autom. Sci. Eng.*, vol. 6, no. 1, pp. 107–120, Jan. 2009.
- [20] J. Yang, D. Zhang, B. Wu, Y. Zhang, and M. Luo, "A path planning method for error region grinding of aero-engine blades with free-form surface," *Int. J. Adv. Manuf. Technol.*, vol. 81, nos. 1–4, pp. 717–728, Oct. 2015.
- [21] Z.-Y. Liao, J.-R. Li, H.-L. Xie, Q.-H. Wang, and X.-F. Zhou, "Region-based toolpath generation for robotic milling of freeform surfaces with stiffness optimization," *Robot. Comput. Integrat. Manuf.*, vol. 64, Aug. 2020, Art. no. 101953.
- [22] J.-W. Ma, X. Lu, G.-L. Li, Z.-W. Qu, and F.-Z. Qin, "Toolpath topology design based on vector field of tool feeding direction in sub-regional processing for complex curved surface," *J. Manuf. Processes*, vol. 52, pp. 44–57, Apr. 2020.
- [23] M. J. B. Fard and H.-Y. Feng, "Effect of tool tilt angle on machining strip width in five-axis flat-end milling of free-form surfaces," *Int. J. Adv. Manuf. Technol.*, vol. 44, nos. 3–4, pp. 211–222, Sep. 2009.
- [24] Y. Han, W.-L. Zhu, L. Zhang, and A. Beauchamp, "Region adaptive scheduling for time-dependent processes with optimal use of machine dynamics," *Int. J. Mach. Tools Manuf.*, vol. 156, Sep. 2020, Art. no. 103589.
- [25] Y. Lv, Z. Peng, C. Qu, and D. Zhu, "An adaptive trajectory planning algorithm for robotic belt grinding of blade leading and trailing edges based on material removal profile model," *Robot. Comput. Integrat. Manuf.*, vol. 66, Dec. 2020, Art. no. 101987.
- [26] H. Chen and N. Xi, "Automated robot tool trajectory connection for spray forming process," *J. Manuf. Sci. Eng.*, vol. 134, no. 2, pp. 1–9, Apr. 2012.
- [27] T. Huang, D. Zhao, and Z.-C. Cao, "Trajectory planning of optical polishing based on optimized implementation of dwell time," *Precis. Eng.*, vol. 62, pp. 223–231, Mar. 2020.
- [28] X. Luo, M. Xiao, Y. Ding, and H. Ding, "Hysteresis modeling and compensation of a pneumatic end-effector based on Gaussian process regression," *Sens. Actuators A, Phys.*, vol. 315, Nov. 2020, Art. no. 112227.
- [29] W. X. Ng, H. K. Chan, W. K. Teo, and I.-M. Chen, "Programming a robot for conformance grinding of complex shapes by capturing the tacit knowledge of a skilled operator," *IEEE Trans. Autom. Sci. Eng.*, vol. 14, no. 2, pp. 1020–1030, Apr. 2017.
- [30] T. Sauer, *Numerical Analysis*, 2nd ed. Boston, MA, USA: Pearson Education, 2011.



Mubang Xiao received the B.S. degree in mechanical engineering from Shanghai Jiao Tong University, Shanghai, China, in 2017, where he is currently pursuing the Ph.D. degree.

His research interests include robotics integrated manufacturing, force control, and contact mechanics.



Ye Ding (Member, IEEE) received the B.S. degree in mechanical engineering from the Nanjing University of Aeronautics and Astronautics, Nanjing, China, in 2003, and the Ph.D. degree in mechanical engineering from Shanghai Jiao Tong University, Shanghai, China, in 2011.

Supported by the Alexander von Humboldt Foundation, he was a Post-Doctoral Scholar at the Laboratory for Precision Machining, University of Bremen, Bremen, Germany, from 2011 to 2012. He joined the School of Mechanical Engineering, Shanghai Jiao Tong University, in 2013, where he is currently a Professor. His research interests include robotics and machining dynamics.

Dr. Ding is an Associate Editor of *Science China Technological Sciences*.



Guilin Yang (Member, IEEE) received the B.E. and M.E. degrees from the Jilin University of Technology, Jilin, China, in 1985 and 1988, respectively, and the Ph.D. degree from Nanyang Technological University, Singapore, in 1999.

He is currently a Professor and the Director of the Zhejiang Key Laboratory of Robotics and Intelligent Manufacturing Equipment Technology, Ningbo Institute of Materials Technology and Engineering, Chinese Academy of Sciences, Ningbo, China. His research interests include mechanism and machine design, modular robotic systems, and robot navigation.